A Computational Fluid Dynamics (CFD)-Based Numerical Investigation of Vehicle Aerodynamic Lift and Drag Characteristics under Variable Boot-Opening Angle and Window Configurations

[1]Adebunmi P. Okediji, [2]Olusola A. Oloruntoba and [3]Akinkunmi P. Akinola
[1]Department of Mechanical Engineering, Elizade University, Ilara-Mokin, Nigeria
[2,3]Department of Automotive Engineering, Elizade University, Ilara-Mokin, Nigeria
adebunmi.okediji@elizadeuniversity.edu.ng | olusola.oloruntoba@elizadeuniversity.edu.ng | akinkunmi.akinola@elizadeuniversity.edu.ng

Received: 17-JULY-2026; Reviewed: 16-SEPT-2026; Accepted: 25-SEPT-2026
https://dx.doi.org/10.46792/fuoyejet.v11i3.1628

ORIGINAL RESEARCH

Abstract— Boot-lid position and cabin-window state are two operationally controllable but under-quantified parameters that govern road-vehicle aerodynamic performance. This study investigates the effects of boot-opening angle on lift and drag coefficients under closed-window (CW) and open-window (OW) configurations. The boot-opening angle was varied from 0° to 90° in 10° increments across seven inlet speeds ranging from 10 to 120 km/h. Computational fluid dynamics (CFD) simulations were conducted using OpenFOAM™. The results indicate that the OW configuration produces a smooth, monotonic decrease in lift coefficient (R^2 = 0.993), reaching a minimum C_L of approximately -1.6 at a boot-opening angle of 90°. Conversely, the CW configuration exhibits a less consistent lift trend (R^2 = 0.7874), characterized by a sharp fluctuation toward zero lift at 60°. The OW configuration consistently generates a higher drag coefficient, with C_d peaking at approximately 0.91 at 90°. In the CW configuration, a substantial drag reduction occurs at 70°, where C_d reaches a local minimum of approximately 0.56, suggesting a geometry-specific optimum for reducing the vehicle wake. A favourable operating point was defined as one that retains at least 75% of the configuration's maximum downforce magnitude while limiting drag to within 20% of its configuration-specific minimum. Based on these criteria, a 40° boot-opening angle under the CW configuration provides the optimal balance between stability ($C_L \cong -0.9$) and aerodynamic efficiency ($C_d \cong 0.65$).

Keywords— Aerodynamic Drag, Aerodynamic Lift, Boot Opening, Closed Window, Open Window, OpenFOAM, CFD.

1 INTRODUCTION

Previous studies have shown that the relationship between vehicle geometry and aerodynamic force coefficients significantly affects vehicle performance, stability, fuel efficiency, and emissions mitigation (Dinh, 2020; Eydgahi & Long, 2011; Gaylard et al., 2014; Good et al., 2011; Howell et al., 2014; Huminic & Huminic, 2017; Jux et al., 2023; Kaleg et al., 2015; Malizia & Blocken, 2021; Mukut & Abedin, 2019; Schuetz, 2016; Urquhart et al., 2020). Katz used the vortex lattice method with freely deforming wake elements to model automotive lifting surfaces near the ground. And evaluated steady and unsteady loads across various wing planforms and found that suspension-induced lift fluctuations on a racing car's front winglet could reach approximately twice the steady-state value (Katz, 1985a). Later, Katz experimentally measured lift and drag on open-wheel racing-car configurations. He found that adding unswept and delta wings to baseline fuselage shapes produced an overall lift coefficient of approximately −1, a result validated against full-scale wind-tunnel data (Katz, 1985b). Heisler explained that lift arises from the pressure difference between the upper-body and underbody airstreams, with its magnitude depending on body styling, underfloor ground clearance, and vehicle speed. Unequal front-to-rear lift alters tyre slip angles, causing understeer or oversteer and reducing road-holding capability and steering stability (Heisler, 2002). Abood and Hussain used computational fluid dynamics (CFD) to optimize a sedan diffuser's ride height, gap, and overlap, achieving a 2.7% reduction in drag and an almost tenfold increase in downforce. These findings confirm that localized rear-body geometry can decouple drag and lift, which is relevant to variations in boot-opening angle (Abood & Hussain, 2024).

These studies progress from vortex-lattice and wind-tunnel analyses of discrete aerodynamic surfaces (Heisler, 2002; Katz, 1985a, 1985b) to CFD-based rear-geometry optimization (Abood & Hussain, 2024), thereby motivating a CFD investigation of boot-opening angle as a comparable parameter influencing the drag and lift coefficients of a minibus under closed-window (CW) and open-window (OW) configurations. However, none of the studies reviewed examines boot-opening angle and cabin-window ventilation state jointly as a parametrically varied CFD design space. Consequently, the interaction between internal cabin airflow and external rear-body geometry remains unquantified.

The present study addresses this gap by extending the boot-opening investigation of previous study (Oloruntoba & Okediji, 2021), which was limited to fuel-consumption and CO_2-emission outcomes, to a CFD-resolved analysis of lift and drag coefficients across seven inlet velocities and two window configurations. Accordingly, this study aims to determine the effect of boot-opening angle on the drag and lift coefficients of a

Corresponding Author: olusola.oloruntoba@elizadeuniversity.edu.ng
Section C- MECHANICAL/MECHATRONICS ENGINEERING & RELATED SCIENCES
Can be cited as:
Okediji A.P., Oloruntoba O.A. and Akinola A. P. (2026). A Computational Fluid Dynamics (CFD)-Based Numerical Investigation of Vehicle Aerodynamic Lift and Drag Characteristics under Variable Boot-Opening Angle and Window (2026). FUOYE Journal of Engineering and Technology (FUOYE**JET), 11(3), 481-489.**
https://dx.doi.org/10.46792/fuoyejet.v11i3.1628

© 2026 The Author(s). Published by Faculty of Engineering, Federal University Oye-Ekiti.
This is an open access article under the CC BY NC license. (https://creativecommons.org/licenses/by-nc/4.0/)

minibus under CW and OW configurations. The investigation is conducted using OpenFOAM™, a well-validated computational fluid dynamics (CFD) software package.

2 COMPUTATIONAL METHODOLOGY

The aerodynamic performance of the vehicle was investigated by analysing the relationship between the boot opening angle (θ) and the resulting aerodynamic forces. The study focused on two primary metrics: the Lift Coefficient (C_L) and the Total Drag Coefficient (C_d). The methodology applied is described presently.

2.1 GEOMETRIC CONFIGURATION OF THE VEHICLE

To investigate the effect of internal cabin airflow on external aerodynamics, numerical simulations were conducted for two distinct vehicle configurations:

1. *Closed Windows* (CW): The vehicle cabin was fully sealed to prevent fluid exchange with the environment. This is the baseline for comparison in this study.
2. *Open Windows* (OW): The vehicle (minibus) windows were open to allow pressure exchange and airflow circulation through the cabin. In the open-window (OW) configuration, all lateral window apertures on both sides of the cabin were modelled as fully open—that is, as part of the fluid domain rather than as solid glazed surfaces. Consequently, the cabin interior formed a single, continuous flow domain with the external flow field. No separate internal inlet or outlet boundary condition was imposed at the window apertures; instead, the far-field boundary conditions described in Section 2.3 were applied to the coupled internal–external flow domain.

The minibus has an overall length $L = 5.915\,m$, width $W = 1.950\,m$ and height $H = 1.990\,m$; it was graphically modelled in OpenSCAD (The Programmers Solid 3D CAD Modeller), version 2021.01 (OpenSCAD, 2021).

In both configurations, i.e. Closed Window and Open Window, the boot opening angle (θ) was varied from $\theta = 0^0$ (fully closed) to $\theta = 90^0$ (fully open), with data points captured at 10^0 increments. Figure (1) shows a pictorial illustration of boot variation.

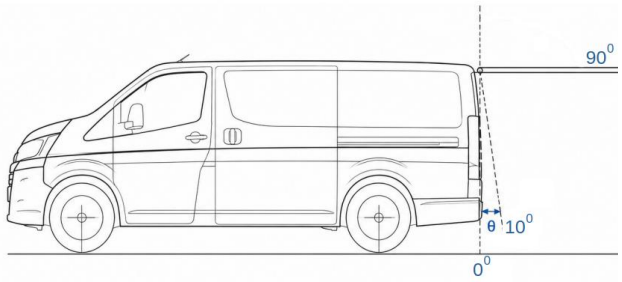

Fig. 1. Pictorial illustration of TOYOTA™ HiAce™ minibus showing boot opening at $\theta = 0^0$, $\theta = 10^0$ and $\theta = 90^0$.

Figures (2a) and (2b) show the minibus with *Closed Window* (CW) and *Open Window* (OW) configurations respectively. The Open Window minibus configuration exposes a driver and ten passengers to complex air flow within the vehicle cabin. This also lead to complex air flow around the vehicle.

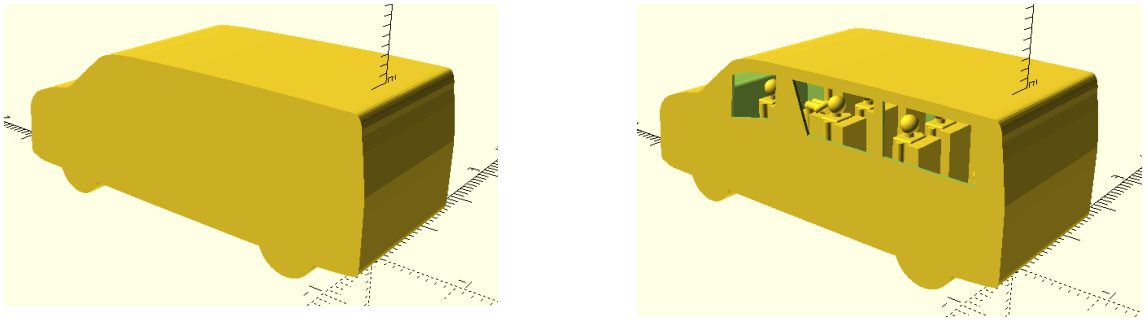

(a) Closed Window (a) Open Window

Fig. 2: Pictorial illustration of TOYOTA™ HiAce™ minibus showing closed and open window.

Table 1. Summary of principal geometric, mesh and numerical-experiment parameters (for reproducibility)

Parameter	Value / definition
Overall length, L	5.915 m
Overall width, W	1.950 m
Overall height, H	1.990 m
Frontal reference area, A_F	3.61 m² (constant across all boot-opening angles)
Boot-opening angle range	0°-90° in 10° increments
Closed Window (CW) configuration	Cabin fully sealed (all windows closed)
Open Window (OW) configuration	All windows open, permitting cabin ventilation and internal-external pressure exchange
Inlet speeds simulated	10, 20, 40, 60, 80, 100, 120 km/h (seven speeds per angle, per configuration)
Total simulation cases	126 (63 CW + 63 OW)
Computational domain dimensions	Length = 9L; Width = 9W; Height = 5L; vehicle positioned 4L downstream of the inlet
Inlet turbulence intensity	1%
Meshing approach	*snappyHexMesh* (OpenFOAM v2412)

© 2026 The Author(s). Published by Faculty of Engineering, Federal University Oye-Ekiti.
This is an open access article under the CC BY NC license. (https://creativecommons.org/licenses/by-nc/4.0/)

http://dx.doi.org/10.46792/fuoyejet.v11i3.1628 engineering.fuoye.edu.ng/journal

Mesh size (CW / OW)	~3.7 million / ~9.9 million cells
Max mesh non-orthogonal quality	64.71 (Good (SciMate-AI, 2026))
Max mesh aspect ratio	8.29 (Good (SciMate-AI, 2026))
Max mesh skewness	3.79 (Acceptable (SciMate-AI, 2026))
Turbulence model	k-ω Shear Stress Transport (SST), RANS
Spatial/temporal discretisation	Second-order; second-order upwind for momentum and turbulence transport equations

In line with previous study (Oloruntoba & Okediji, 2021), the numerical wind tunnel employed in this study extends 9L in length and 9W in width, with a height of 5L; the vehicle is positioned 4L downstream of the domain inlet, leaving sufficient distance downstream to capture wake development without artificial confinement from the outlet boundary. Table (1) summarises these and other principal geometric, meshing and numerical-experiment parameters for the purpose of reproducibility.

2.2. GOVERNING EQUATIONS

The Navier-Stokes equations (NSE) is the mathematical foundation for Computational Fluid Dynamics (CFD), hence, it formed the basis for aerodynamic analysis in this study. Equations (1) and (2) show the equations of conservation of mass and momentum respectively, which form the NSE (ANSYS, 2016; C. Zhang et al., 2019). The symbols in the equations include: $\vec{v}$, ρ, P, $\bar{\bar{\tau}}$ and $\rho\vec{g}$, which symbolise velocity vector, density, static pressure, stress tensor, and gravitational body force respectively. Turbulence, which becomes significant at high Reynold's number, is modelled in the NSE via the SST $k-\omega$ viscous model.

$$\frac{\partial \rho}{\partial t} + \nabla \cdot (\rho \vec{v}) = 0 \quad (1)$$

$$\frac{\partial (\rho \vec{v})}{\partial t} + \nabla \cdot (\rho \vec{v}\vec{v}) = -\nabla P + \nabla \cdot (\bar{\bar{\tau}}) + \rho \vec{g} \quad (2)$$

2.3. BOUNDARY CONDITIONS

This study utilised a numerical wind tunnel which is sufficiently large to accurately capture the aerodynamics of the vehicle under consideration (Ashton & Revell, 2015; C. Zhang et al., 2019). The principal boundary conditions were as follows: (a) a velocity inlet with a prescribed value equal to the vehicle speed, representing practical on-road conditions, and (b) a pressure outlet set to atmospheric pressure. To reproduce relative vehicle–road motion, the ground was modelled as a moving wall with a velocity equal to the inlet velocity. The remaining domain boundaries—namely, the top and two side boundaries—were treated as symmetry planes. A turbulence intensity of 1% was prescribed at the inlet, consistent with typical low-turbulence, open-road conditions.

The steady Reynolds-averaged Navier–Stokes (RANS) k–ω shear-stress transport (SST) turbulence model was adopted because it is widely used for bluff-body road-vehicle flows and provides a suitable balance between accuracy and computational cost for the 126-case parametric matrix considered in this study. Nevertheless, at larger boot-opening angles ($\theta \geq 70°$), where strong flow separation occurs at the boot lid, some fluctuations in the CW lift trend reported in Section 3.1 may arise from underlying flow unsteadiness that steady RANS can represent only in a time-averaged manner. Applying a scale-resolving approach, such as detached-eddy simulation (DES) or large-eddy simulation (LES), to selected high-angle cases could help quantify this effect and is therefore recommended for future work.

A total of 126 simulation cases were carried out in this study; 63 of the simulation cases were for each of closed window and open window configurations respectively. For each geometric configuration (i.e. OW/CW): (a) inlet velocities considered include: 10 km/h, 20 km/h, 40 km/h, 60 km/h, 80 km/h, 100 km/h and 120 km/h, (b) boot openings considered include: range 0^0 – 90^0 in increment of 10^0.

2.4. MESHING AND NUMERICAL DISCRETIZATION

Meshing of the geometric computational domain is accomplished using the *snappyHexMesh* in OpenFOAM (v2412) to achieve good gradient approximations, reasonable convergence speed and computational time.

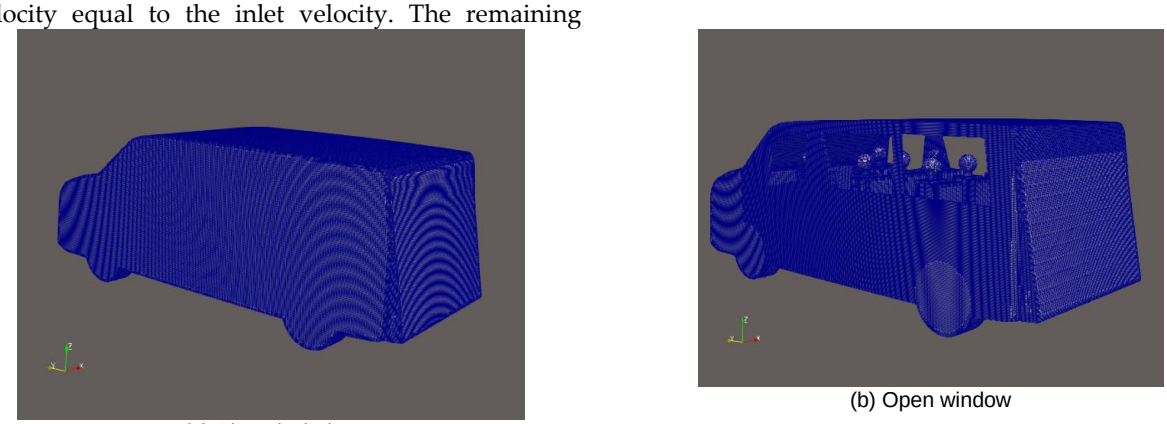

(a) Closed window (b) Open window

Fig. 3: Mesh of the minibus with 10° open boot under closed- and open-window configurations

© 2026 The Author(s). Published by Faculty of Engineering, Federal University Oye-Ekiti.
This is an open access article under the CC BY NC license. (https://creativecommons.org/licenses/by-nc/4.0/)

http://dx.doi.org/10.46792/fuoyejet.v11i3.1628 engineering.fuoye.edu.ng/journal

The OpenFOAM™ program was applied to numerically discretise the governing equations, given in Equations (1) and (2), using the well-established finite volume method (FVM) scheme (Caramia & Distaso, 2025; Ricci, 2025; Weller et al., 1998). In order to improve solution accuracy, spatial discretization was set to second-order. Also, second-order upwind was applied to momentum equations (Álvarez et al., 2023; Deng et al., 2023; Jiang et al., 2024). The k–ω Shear Stress Transport (SST) model is applied to capture turbulence (Sakamoto et al., 2024; Wang et al., 2024; Zhu et al., 2023). Furthermore, numerical discretisation of turbulence transport equations was achieved via a second-order upwind scheme.

2.5. DRAG AND LIFT COEFFICIENTS

Based on standard approach for vehicle performance model operating on horizontal road with negligible inertia (X. Zhang & Mi, 2011), drag coefficient is determined as $C_d = 2F_d/\rho A_F v^2$. A similar expression describes lift coefficient as $C_L = 2F_L/\rho A_L v^2$.

2.6. DATA ACQUISITION AND PROCESSING

The coefficients for lift and drag were recorded for each angle. The datasets utilized for analysis were labelled as *Average-CL* and *Average-Cd*, since multiple measurements were taken at each boot opening to ensure a representative mean value. In particular, C_L and C_d were measured at seven specific speeds: 10, 20, 40, 60, 80, 100, and 120 km/h. however, the values used for computing *Average-CL* and *Average-Cd* are values of C_L and C_d corresponding to 60, 80, 100, and 120 km/h. This is due to the fact that, drag coefficient becomes practically important or relevant in terms of energy losses from vehicle speed 60 km/h.

2.7. STATISTICAL ANALYSIS AND CURVE FITTING

To determine the mathematical relationship between the boot angle and aerodynamic coefficients, a *non-linear regression* was performed on each dataset. A *fourth-order polynomial function* was employed for the fit as $Function = a_0 + a_1x + a_2x^2 + a_3x^3 + a_4x^4$; where x represents the boot opening angle in degrees. The precision and reliability of these mathematical models were evaluated using the following statistical parameters:

1. **Reduced Chi-Square (χ^2/doF):** Used to assess the goodness of fit.
2. **Coefficient of Determination (R^2):** Used to measure how well the regression model explains the variance in the experimental data.
3. **Parameter Estimates (a_0 through a_4):** Calculated with associated standard errors to define the specific curvature of the lift and drag trends for both the CW and OW configurations.

3. RESULTS AND DISCUSSION

The aerodynamic impact of varying the boot opening angle (θ) was evaluated via CFD analysis leading to the quantification of *lift coefficient* (C_L) and *total drag coefficient* (C_d) under two distinct configurations: *Closed Windows* (CW) and *Open Windows* (OW). The results, illustrated in the provided figures, reveal a complex relationship between vehicle geometry and aerodynamic forces; these are examined presently.

3.1. PRESENTATION AND ANALYSIS OF LIFT COEFFICIENT (C_L)

The lift coefficient data, presented in Figure (4), shows that the vehicle generally experiences negative lift (or positive downforce) across the entire range of boot opening angles; this is consistence with expected pattern for land vehicles needed to achieve tire grip, manoeuvrability and overall vehicle stability (Abood & Hussain, 2024; Heisler, 2002). Specific observations include:

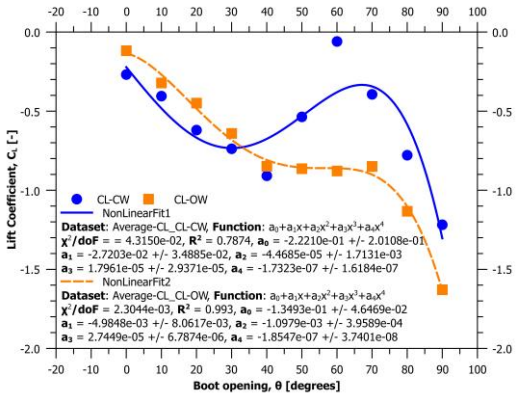

Fig. 4. Variation of the lift coefficient (C_L) as a function of the boot opening angle (θ) for *Closed Window* (CW) and *Open Window* (OW)

1. **Trends in CW vs. OW:** For the *Closed Window* (CW) configuration, the coefficient of lift initially decreases as the boot opening increases, reaching a local minimum of lift coefficient near $\theta = 40^0$ ($C_L \cong -0.9$). Interestingly, a significant fluctuation occurs between $\theta = 50^0$ and $\theta = 70^0$, where C_L rises sharply toward zero at $\theta = 60^0$ before dropping again.
2. **Effect of Open Windows:** The *Open Windows* (OW) configuration exhibits a more consistent trend. While it starts with higher lift coefficient at $\theta = 0^0$ compared to CW, it eventually attained significantly lower lift coefficient at higher angles. At $\theta = 90^0$ boot opening, the OW configuration reaches its minimum lift coefficient at $C_L = -1.6$, whereas the CW configuration is notably higher at $C_L = -1.2$.
3. **Statistical Fit:** The non-linear polynomial fit for the OW data is close, with an R^2 value of 0.993, indicating a smooth, monotonic progression of lift as the boot opens. In contrast, the CW data ($R^2 = 0.7874$) suggests a less smooth flow behaviour, likely due to complex pressure interactions when the cabin is sealed.

Physically, the progressive decrease in lift coefficient with increasing boot-opening angle is consistent with the boot lid increasingly acting as an inclined rear deflector. As θ increases, the lid presents a larger projected area to the airflow approaching from the underbody and roof,

© 2026 The Author(s). Published by Faculty of Engineering, Federal University Oye-Ekiti.
This is an open access article under the CC BY NC license. (https://creativecommons.org/licenses/by-nc/4.0/)

http://dx.doi.org/10.46792/fuoyejet.v11i3.1628 engineering.fuoye.edu.ng/journal

thereby redirecting the wake flow and modifying the pressure distribution over the rear of the vehicle. The resulting reduction in pressure over the upper rear surface relative to the underbody increases downforce, producing a more negative lift coefficient.

In the CW configuration, the sealed cabin requires the external boundary-layer flow to pass entirely over the roof–boot-lid junction. At intermediate angles (θ = 50°–70°), the geometry may approach a critical condition for flow separation under the local adverse pressure gradient. Consequently, small changes in θ may shift the separation point and produce the non-monotonic lift response—and corresponding lower R^2 value. In the OW configuration, internal cabin airflow provides an additional, comparatively stable flow path that bypasses the external roof–boot-lid junction. This mechanism is consistent with the smoother and more monotonic lift trend observed. However, direct confirmation would require pressure-field or streamline data at the roof–boot-lid junction. Scale-resolving simulations are therefore recommended in Section 2.3 as a focus for future work.

3.2. PRESENTATION AND ANALYSIS OF DRAG COEFFICIENT (C_d)

The drag coefficient, presented in Figure (5), highlights the efficiency trade-off associated with different boot positions and window opening states. Specific observations include:

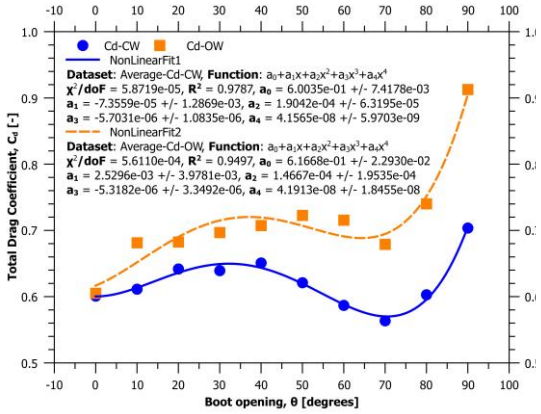

Fig. 5. Variation of the drag coefficient (C_d) as a function of the boot opening angle (θ) for *Closed Window* (CW) and *Open Window* (OW)

1. **Base Drag:** At a fully closed position ($\theta = 0^0$), both *Closed Window* (CW) and *Open Window* (OW) configurations start with a similar C_d of approximately 0.6; the actual values, however, show that C_d for OW configuration is higher at 0.605 compared to 0.601 for CW configuration.
2. **Drag Penalty of Open Windows:** As the boot angle increases, the *Open Windows* (OW) configuration consistently produces higher drag than the CW configuration. This is particularly evident at $\theta = 90^0$, where the OW drag spikes to approximately 0.91, representing a substantial increase in air resistance compared to the CW value of approximately 0.7.
3. **Efficiency Peaks:** For the *Closed Windows* (CW) setup, a notable "dip" in drag occurs at $\theta = 70^0$ ($C_d \cong 0.56$), suggesting a geometric alignment that minimizes the wake area and optimising flow reattachment at that specific angle. This is consistent with a previous study that shows minimum value of C_d in the same vicinity of θ (Oloruntoba & Okediji, 2021)*Open Window* (OW) configuration, but at a higher value than the base drag.

The drag response is consistent with the boot lid acting as a bluff obstruction. As the lid rotates upward, it increasingly obstructs the rear flow, enlarging the separated wake and increasing pressure (form) drag. This behaviour explains the general rise in drag coefficient as θ approaches 90° in both configurations.

The local minimum in drag at θ = 70° under the CW configuration may indicate a flow-reattachment effect. At this angle, the boot-lid geometry may align the separated shear layer such that it temporarily reattaches to the lid surface rather than shedding directly into a broad wake. This effect would reduce the effective wake cross-sectional area and, consequently, the pressure-drag penalty. The trend then reverses as the lid approaches the fully vertical position at θ = 90° .

The consistently higher drag observed in the OW configuration may be attributed to the cabin providing an additional internal airflow path. Air entering through the open windows is subsequently discharged into the rear flow, where it interacts with the external separated wake. This interaction may increase wake mixing and associated aerodynamic losses, thereby intensifying the boot-lid blockage effect rather than alleviating it. Direct pressure-field, mass-flow, or streamline data would be required to confirm this proposed mechanism.

3.3. EFFECT OF INLET SPEED ON AERODYNAMIC COEFFICIENTS

Sections 3.1 and 3.2 reported lift and drag coefficients averaged over the four highest simulated speeds (60-120 km/h), consistent with typical open-road operation. The full dataset, however, spans seven inlet speeds (10-120 km/h) at every boot-opening angle, which allows the speed-dependence of the coefficients to be examined directly rather than assumed. Figure (6) plots C_d and C_L against speed for four representative boot-opening angles (0deg, 40deg, 70deg and 90deg) in both configurations. Two patterns emerge. First, both configurations exhibit their greatest speed-to-speed variation at the lowest simulated speed (10 km/h),

© 2026 The Author(s). Published by Faculty of Engineering, Federal University Oye-Ekiti.
This is an open access article under the CC BY NC license. (https://creativecommons.org/licenses/by-nc/4.0/)

http://dx.doi.org/10.46792/fuoyejet.v11i3.1628 engineering.fuoye.edu.ng/journal

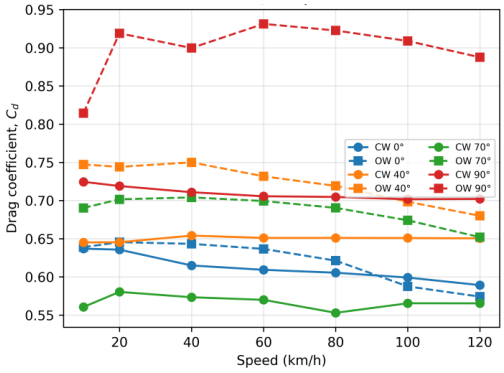

(a) Drag coefficient

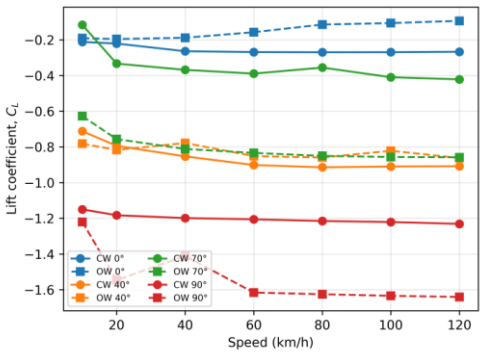

(b) Lift coefficient

Fig. 6: Effect of inlet speed on drag coefficient and lift coefficient, at four representative boot-opening angles, for Closed Window (CW) and Open Window (OW) configurations

after which the coefficients approach a comparatively stable plateau above approximately 40–60 km/h. This behaviour is consistent with a flow regime that is still developing at low Reynolds numbers and stabilises as speed increases, rather than with an artefact of a single operating condition. Second, sensitivity to speed is not uniform across boot-opening angle or configuration. The OW lift coefficient becomes markedly more speed-sensitive as the boot opens further, with the spread across the seven simulated speeds increasing from 0.10 at 0° to 0.42 at 90°. By contrast, the CW drag coefficient remains comparatively insensitive to speed at all angles, with its largest spread being only 0.065 at 10°. Notably, the CW lift coefficient near 60° remains close to zero across the full speed range; the spread reaches 0.31 at 70°, rather than occurring only at the single speed used to calculate the configuration average. This confirms that the near-zero-lift fluctuation reported in Section 3.1 is a genuine, repeatable feature of the CW flow at that angle, rather than a numerical outlier at one operating speed.

3.4. COUPLED INTERPRETATION OF CLOSED WINDOW AND OPEN WINDOW CONFIGURATIONS

Considered jointly, the CW and OW results indicate that window state and boot-opening angle do not act independently; instead, they modulate the same underlying separation and wake mechanism through two distinct flow paths. Boot-opening angle primarily governs external separation at the rear of the vehicle (Sections 3.1–3.2), whereas window state determines whether an internal cabin-flow path is available to interact with this external separation.

When the cabin is sealed (CW), the boot-lid junction is the principal flow feature governing both lift and drag. Its sensitivity to θ is therefore expressed directly in the CW response, including the non-monotonic lift variation and the local drag minimum near 70°. When the windows are open (OW), the internal cabin path introduces a second, comparatively steady momentum source that (i) smooths the lift response, yielding a higher R^2 value (0.993, compared with 0.7874), by providing a consistent counteracting flow, but (ii) increases drag at every angle beyond θ = 0° by adding to the mass and momentum that must pass through the already separated rear wake.

This coupling explains why the two configurations cannot be ranked simply as "better" or "worse." OW is preferable when predictable, high-magnitude downforce is the priority, whereas CW is preferable when drag—and, consequently, fuel or energy consumption—is the binding constraint. The CW operating point at θ = 40° (Section 3.5) therefore represents a practical compromise between these competing objectives.

To probe the coupling mechanism proposed above more directly, Figures (7) and (8) show instantaneous Q-criterion iso-surfaces and cabin-region streamlines for the CW and OW configurations at a representative boot-opening angle of 40deg.

The corresponding streamlines (Figure 8) reinforce this interpretation. In the CW configuration, the external flow passes over the sealed cabin and separates from the boot lid in a comparatively organised manner. In the OW configuration, by contrast, streamlines enter the cabin through the window apertures, circulate around the seating geometry, and re-emerge to interact with the external rear-wake flow. This behaviour provides a flow-visualisation basis for the proposed explanation of why the OW configuration increases, rather than alleviates, the drag associated with boot-lid blockage.

3.5. ESTIMATED AERODYNAMIC FORCES

Coefficients alone do not convey the physical magnitude of the aerodynamic loads on the vehicle. The drag force was computed as $F_d = C_d \rho A_F v^2/2$, using the constant frontal reference area ($A_F = 3.61\, m^2$) and standard sea-level air density ($\rho = 1.225\, kg/m^3$). The corresponding lift force was computed as $F_L = C_d \rho A_L v^2/2$, using a lift-relevant reference area A_L that varies with boot-opening angle, since the boot lid itself contributes to the projectedarea seen by the flow; A_L was obtained by summing the fixed vehicle planform area with the additional sector area swept by the boot lid at each opening angle (Table 2). Both forces are evaluated at a representative highway reference speed of 100 km/h using the full per-speed

© 2026 The Author(s). Published by Faculty of Engineering, Federal University Oye-Ekiti.
This is an open access article under the CC BY NC license. (https://creativecommons.org/licenses/by-nc/4.0/)

http://dx.doi.org/10.46792/fuoyejet.v11i3.1628 engineering.fuoye.edu.ng/journal

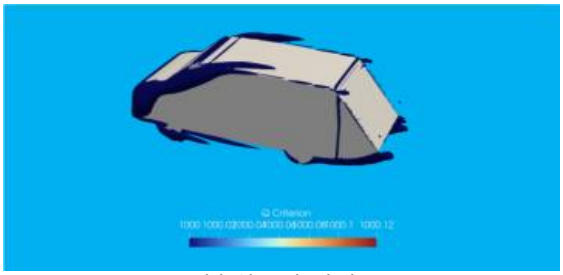

(a) Closed Window

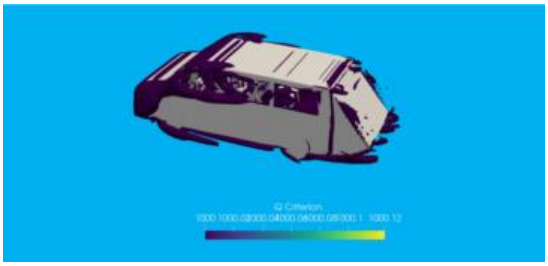

(a) Open Window

Fig. 7. Instantaneous Q-criterion iso-surfaces

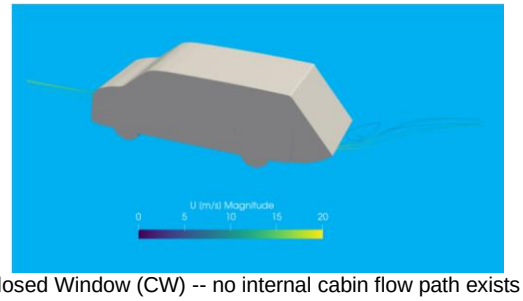

(a) Closed Window (CW) -- no internal cabin flow path exists in this configuration, so streamlines shown here are confined to the external flow;

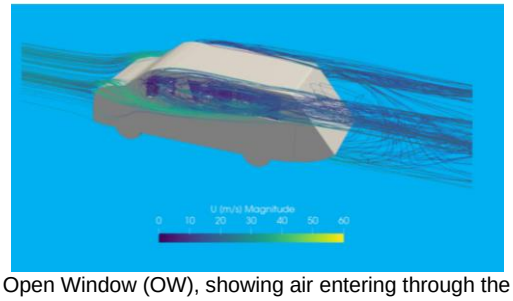

(b) Open Window (OW), showing air entering through the open windows

Fig. 8. Streamlines in the cabin region at theta = 40deg boot opening:

Table 2. Lift reference area (A_L) by boot-opening angle, with the corresponding lift coefficients at 100 km/h

Boot-opening angle (degree)	Lift reference area, A_L (m²)	CW C_L @100 km/h	OW C_L @100 km/h
0	10.04	-0.269	-0.106
10	10.58	-0.411	-0.322
20	11.10	-0.622	-0.460
30	11.58	-0.742	-0.643
40	12.03	-0.910	-0.822
50	12.41	-0.546	-0.862
60	12.71	-0.090	-0.901
70	12.94	-0.410	-0.857
80	13.08	-0.788	-1.148
90	13.13	-1.221	-1.634

Table 3. Estimated drag and lift forces by boot-opening angle and configuration, at a reference speed of 100 km/h

Boot angle (degree)	CW F_D (N)	OW F_D (N)	CW F_L (N)	OW F_L (N)	CW F_L/F_D	OW F_L/F_D
0	1022	1003	-1278	-504	1.25	0.50
10	1035	1181	-2054	-1610	1.98	1.36
20	1094	1149	-3260	-2415	2.98	2.10
30	1091	1163	-4063	-3521	3.73	3.03
40	1111	1192	-5172	-4672	4.66	3.92
50	1060	1224	-3202	-5058	3.02	4.13
60	1004	1220	-544	-5413	0.54	4.44
70	965	1150	-2505	-5238	2.60	4.55
80	1029	1260	-4871	-7097	4.74	5.63
90	1197	1551	-7576	-10141	6.33	6.54

dataset (Section 3.3), rather than the configuration-average coefficients, so the values below are directly grounded in the simulation output at that speed.

At 100 km/h, the drag force ranges from approximately 965 to 1197 N across the CW angle range and reaches 1551 N for the OW configuration at 90°, representing an increase of approximately 52% relative to the closed-boot CW baseline. Because A_L increases with boot-opening angle while |CL| increases concurrently, the estimated lift, or downforce, grows faster than drag. At 90°, the downforce reaches approximately 7576 N for CW and 10,141 N for OW—approximately 6.3 and 6.5 times their respective drag forces. The resulting lift-to-drag ratios are reported in Table (3) for every angle and configuration. These ratios provide a more physically direct basis for comparing the configurations than the coefficients alone because, unlike the coefficients, they are independent of the selected reference area.

3.6. INTERPRETATION AND SYNTHESIS

The data suggest that the boot lid functions as a powerful aerodynamic control surface. At high opening angles, particularly near (near $\theta = 90^0$), it behaves similarly to a spoiler or air brake by substantially increasing the drag coefficient while producing greater downforce. The Open Windows (OW) configuration allows air to circulate through the cabin, which further enhances the downforce

© 2026 The Author(s). Published by Faculty of Engineering, Federal University Oye-Ekiti.
This is an open access article under the CC BY NC license. (https://creativecommons.org/licenses/by-nc/4.0/)

http://dx.doi.org/10.46792/fuoyejet.v11i3.1628 engineering.fuoye.edu.ng/journal

effect but incurs a substantial drag penalty. The sharp increase in drag observed for OW at $\theta = 90^0$ indicates that the combined effect of the open cabin and vertically oriented boot lid produces a highly turbulent, high-pressure stagnation region at the rear of the vehicle.

For practical applications, when the objective is to maintain vehicle stability through high downforce while limiting drag, the Closed Windows (CW) configuration at a boot-opening angle of approximately $\theta = 40^0$ appears to offer a favourable compromise. At this operating point, it provides substantial downforce ($C_L \cong -0.9$) with comparatively moderate drag ($C_d \cong 0.65$).

4 CONCLUSION

This study successfully employed Computational Fluid Dynamics (CFD) to characterise the aerodynamic performance of a vehicle with varying boot-opening angles under Closed Window (CW) and Open Window (OW) conditions. The results demonstrate that the boot lid functions as an aerodynamic control surface, with its effects on lift and drag strongly influenced by the vehicle's window state, as discussed in Section 3.3. The primary findings of this study are as follows:

1. *Aerodynamic Lift and Stability:* The *Open Window* configuration provides a smooth, monotonic decrease in lift coefficient, well described by a fourth-order polynomial fit ($R^2 = 0.993$). At a fully open angle of 90°, the OW state achieves a minimum lift coefficient of approximately -1.6. Conversely, the *Closed Window* (CW) configuration displays a less smooth lift trend ($R^2 = 0.7874$), characterized by a significant fluctuation toward zero lift at a 60° angle.
2. *Drag and Efficiency:* In terms of aerodynamic resistance, the Open Window configuration consistently generates higher drag coefficient than the *Closed Window* configuration, reaching a peak coefficient of drag of approximately 0.91 at 90°. Notably, the CW configuration demonstrates a specific point of geometric optimization at 70°, where the drag coefficient reaches a local minimum of approximately 0.56, suggesting a reduction in the vehicle's wake area at this specific orientation.
3. *Operational Optimization:* The data indicate that a 40° boot opening in the Closed Window configuration satisfies the balance criterion defined in this study: it retains at least 75% of the configuration's maximum downforce magnitude while keeping drag within 20% of its configuration-specific minimum. This operating point therefore provides substantial aerodynamic stability, with a lift coefficient of approximately (-0.9), while maintaining a relatively efficient drag coefficient of approximately (0.65).

The principal scientific contribution of this study is the demonstration that boot-opening angle and cabin-window state function as coupled, rather than independent, aerodynamic control parameters (Section 3.4). Window state does not merely shift the lift and drag levels produced by the boot angle; it also modifies the smoothness and, in some cases, the qualitative form of the boot-angle response itself.

continue

Ultimately, these results highlight the complex interplay between internal cabin airflow and external rear-end geometry, providing a foundation for the development of active aerodynamic systems designed to enhance vehicle stability and efficiency.

REFERENCES

Abood, M. S., & Hussain, I. (2024). Ground effect of an inverted double element wing diffuser on a sedan car. Heliyon, 10(8), e29435. https://doi.org/10.1016/j.heliyon.2024.e29435

Álvarez, A. J., Nieto, F., Kwok, K. K. C. S., & Hernández, S. (2023). A simplified CFD approach for bluff-body aerodynamics under small scale free stream turbulent flow. Journal of Wind Engineering and Industrial Aerodynamics, 241, 105500. https://doi.org/10.1016/j.jweia.2023.105500

ANSYS. (2016). ANSYS FLUENT Theory Guide (17.0). ANSYS, Inc.

Ashton, N., & Revell, A. (2015). Comparison of RANS and DES Methods for the DrivAer Automotive Body Comparison of RANS and DES Methods for the DrivAer Automotive Body. SAE International. https://doi.org/10.4271/2015-01-1538

Caramia, G., & Distaso, E. (2025). The Finite Volume Method. In G. Caramia & E. Distaso (Eds.), A Practical Approach to Computational Fluid Dynamics Using OpenFOAM® (pp. 79–124). Springer Nature Switzerland. https://doi.org/10.1007/978-3-031-88957-8_3

Deng, X., Massey, J. C., & Swaminathan, N. (2023). Large-eddy simulation of bluff-body stabilized premixed flames with low-dissipative, structure-preserving convection schemes. AIP Advances, 13(5), 055014. https://doi.org/10.1063/5.0155829

Dinh, T. Q. (2020). Intelligent and Efficient Transport Systems—Design, Modelling, Control and Simulation. https://doi.org/10.5772/intechopen.81308

Eydgahi, A., & Long, E. L. (2011). Converting an Internal Combustion Engine Vehicle to an Electric Vehicle. 22.381.1-22.381.15. https://peer.asee.org/converting-an-internal-combustion-engine-vehicle-to-an-electric-vehicle

Gaylard, A. P., Oettle, N., Gargoloff, J., & Duncan, B. (2014). Evaluation of Non-Uniform Upstream Flow Effects on Vehicle Aerodynamics. SAE International, 692–702. https://doi.org/10.4271/2014-01-0614

Good, G. L., Johnson, C., Clough, B., & Lewis, R. (2011). The Aesthetics of Low Drag Vehicles. SAE International. https://doi.org/10.4271/2011-37-0016

Heisler, H. (2002). 14—Vehicle body aerodynamics. In Advanced Vehicle Technology (Second Edition) (pp. 584–634). Butterworth-Heinemann. https://doi.org/10.1016/B978-075065131-8/50015-4

Howell, J., Garry, K., & Holt, J. (2014). The Aerodynamics of a Small Car Overtaking a Truck Tata Motors European Technical Centre. SAE International. https://doi.org/10.4271/2014-01-0604

Huminic, A., & Huminic, G. (2017). Aerodynamic Study of a Generic Car Model with Wheels and Underbody Diffuser. International Journal of Automotive Technology, 18(3), 397–404. https://doi.org/10.1007/s12239-017-0040-6

Jiang, P., Huang, Y., Cao, Y., Liao, S., & Xie, B. (2024). Utility of High-order Scheme for Unsteady Flow Simulations: Comparison with Second-order Tool. https://arxiv.org/abs/2407.19764

Jux, C., Sciacchitano, A., & Scarano, F. (2023). Tire dependence for the aerodynamics of yawed bicycle wheels. Journal of Wind Engineering and Industrial Aerodynamics, 233, 105294. https://doi.org/10.1016/j.jweia.2022.105294

Kaleg, S., Hapid, A., & Kurnia, M. R. (2015). Electric Vehicle Conversion Based on Distance, Speed and Cost Requirements.

© 2026 The Author(s). Published by Faculty of Engineering, Federal University Oye-Ekiti.
This is an open access article under the CC BY NC license. (https://creativecommons.org/licenses/by-nc/4.0/)

Energy Procedia, 2nd International Conference on Sustainable Energy Engineering and Application (ICSEEA) 2014 Sustainable Energy for Green Mobility, 68, 446–454. https://doi.org/10.1016/j.egypro.2015.03.276

Katz, J. (1985a). Calculation of the Aerodynamic Forces on Automotive Lifting Surfaces. Journal of Fluids Engineering, 107(4), 438–443. https://doi.org/10.1115/1.3242507

Katz, J. (1985b). Investigation of Negative Lifting Surfaces Attached to an Open-Wheel Racing Car Configuration. SAE International. SAE International Congress and Exposition. https://doi.org/10.4271/850283

Malizia, F., & Blocken, B. (2021). Cyclist aerodynamics through time: Better, faster, stronger. Journal of Wind Engineering and Industrial Aerodynamics, 214, 104673. https://doi.org/10.1016/j.jweia.2021.104673

Mukut, M. I., & Abedin, M. Z. (2019). Review on Aerodynamic Drag Reduction of Vehicles. International Journal of Engineering Materials and Manufacture, 4(1), 1–14.

Oloruntoba, O. A., & Okediji, A. P. (2021). Effect of Speed and Boot Opening on Aerodynamics, Fuel Consumption, and CO2 Emission of Minibus. FUOYE Journal of Engineering and Technology, 6(4). https://doi.org/10.46792/fuoyejet.v6i4.665

OpenSCAD. (2021). OpenSCAD (Version 2021.01) [Computer software]. https://www.openscad.org

Ricci, A. (2025). Review of OpenFOAM applications in the computational wind engineering: From wind environment to wind structural engineering. Meccanica, 60(6), 1695–1735. https://doi.org/10.1007/s11012-024-01826-x

Sakamoto, N., Hino, T., Kobayashi, H., & Ohashi, K. (2024). Parameter adaptation of k − ω SST turbulence model for improving resolution of moderately separated flows around 2D wing and 3D ship hulls via EnKF data assimilation. Journal of Marine Science and Technology, 29(4), 885–909. https://doi.org/10.1007/s00773-024-01026-y

Schuetz, T. (2016). Aerodynamics of Road Vehicles. SAE International.

SciMate-AI. (2026). HPC-Skills/skills/hpc-openfoam/references/mesh-quality-and-generation-guide.md at main · SciMate-AI/HPC-Skills. GitHub. https://github.com/SciMate-AI/HPC-Skills/blob/main/skills/hpc-openfoam/references/mesh-quality-and-generation-guide.md

Urquhart, M., Varney, M., Sebben, S., & Passmore, M. (2020). Aerodynamic drag improvements on a square-back vehicle at yaw using a tapered cavity and asymmetric flaps. International Journal of Heat and Fluid Flow, 86, 108737. https://doi.org/10.1016/j.ijheatfluidflow.2020.108737

Wang, C., Sun, M., Yang, Y., Wang, H., Liu, X., Xiong, D., & Wang, Y. (2024). Improved SST turbulence model for supersonic flows with APG/separation. Computers & Fluids, 274, 106237. https://doi.org/10.1016/j.compfluid.2024.106237

Weller, H. G., Tabor, G., Jasak, H., & Fureby, C. (1998). A tensorial approach to computational continuum mechanics using object-oriented techniques. Computer in Physics, 12(6), 620–631. https://doi.org/10.1063/1.168744

Zhang, C., Bounds, C. P., Foster, L., & Uddin, M. (2019). Turbulence Modeling Effects on the CFD Predictions of Flow over a Detailed Full-Scale Sedan Vehicle. Fluids, 4(148), 1–28. https://doi.org/10.3390/fluids4030148

Zhang, X., & Mi, C. (2011). Vehicle Power Management: Modelling, Control and Optimization. Springer. https://doi.org/10.1007/978-0-85729-736-5

Zhu, L., Wang, T., Guo, Q., & Yuan, X. (2023). NN-augmented k-ω shear stress transport turbulence model for high-speed flows with shock-wave/boundary layer interaction. Engineering Applications of Computational Fluid Mechanics, 17(1), 2374316. https://doi.org/10.1080/19942060.2024.2374316

© 2026 The Author(s). Published by Faculty of Engineering, Federal University Oye-Ekiti.
This is an open access article under the CC BY NC license. (https://creativecommons.org/licenses/by-nc/4.0/)